We thus expect the explanation for the repulsive hydrodynamic interaction to lie in the realm of viscosity-dominated flows, where small inertial effects are probably significant. There are only a few analytical results available for a force-free particle in a wall-bounded shear flow[30]: such a particle experiences a lift force transverse to the streamlines $O(\mu u_C a \mathrm{Re}_G)$, where u_C is the typical velocity on the scale of the particle, and $\mathrm{Re}_G = \rho G a^2/\mu$ is the Reynolds number based on the local shear rate G. For our system, the particle experiences a torque, which generates a local velocity $u_C = \omega a$, and the background shear rate is $G = O(\omega a^3/d^3)$, where d is the distance between the centres of the disks. Therefore, the repulsive hydrodynamic force F_h between the disks is predicted to be $F_h = O(\mu(\omega a)a\mathrm{Re}_G) = O(\rho \omega^2 a^7/d^3)$. In the stable configuration, this hydrodynamic repulsion balances the magnetic force attracting the disks towards the axis of rotation of the external magnet. Although a detailed calculation remains to be done, we verified experimentally that qualitative trends predicted by this analysis appear to be correct (see Supplementary Information).

Our qualitative theory explains the nature of the pairwise forces acting in the system, but it is clearly insufficient to account for the emergence of the patterns that we observe, especially in more complicated systems. The structure of the aggregates of disks of different sizes can be controlled by adjusting the rotational speed to decouple larger disks from the field selectively (Fig. 4a). Aggregates that have structures dependent on the initial distribution of the disks can also be prepared (Fig. 4b). The self-assembly can take place on both planar and curved surfaces (Fig. 4c). It seems likely that changing the shape of the spinners, and engineering the profile of the magnetic field, would lead to even more complex behaviour.

We believe that this system could be a useful experimental tool in assisting theoretical research on multivortex flows. Also, if the size of the disks could be reduced to several micrometres, the type of self-assembly that we describe here might have practical applications in optics; for example, in tunable diffraction gratings or in photonic bandgap materials. If it was found to be possible to 'solidify' large, dynamic structures, new materials or materials precursors (such as membranes and molecular sieves) might be obtained. □

1. Mayer, A. M. Floating magnets. *Nature* **18**, 258–260 (1878).
2. Derr, L. A photographic study of Mayer's floating magnets. *Proc. Am. Acad. Arts Sci.* **44**, 525–528 (1909).
3. Monckman, J. On the arrangement of electrified cylinders when attracted by an electrified sphere. *Proc. Camb. Phil. Soc.* **6**, 179–181 (1888).
4. Schecter, D. A., Dubin, D. H. E., Fine, K. S. & Driscoli, C. F. Vortex crystals from 2D Euler flow: experiment and simulation. *Phys. Fluids* **11**, 905–914 (1999).
5. Bubeck, R., Bechinger C., Neser, S. & Leiderer, P. Melting and reentrant freezing of two-dimensional colloidal crystals in confined geometry. *Phys. Rev. Lett.* **82**, 3364–3367 (1999).
6. Ghyka, M. *The Geometry of Art and Life* (Dover, New York, 1977).
7. Ball, P. *The Self-Made Tapestry: Pattern Formation in Nature* (Oxford Univ. Press, New York, 1999).
8. Whitesell, J. K. *Organised Molecular Assemblies in the Solid State* (Wiley, New York, 1999).
9. Philp, D. & Stoddart, J. F. Self-assembly in natural and unnatural systems. *Angew. Chem. Int. Edn Engl.* **35**, 1155–1196 (1996).
10. Lounasmaa, O. V. & Thuneberg, E. Vortices in rotating superfluid ³He. *Proc. Natl Acad. Sci. USA* **96**, 7760–7767 (1999).
11. Bowden, N., Brittain, S., Evans, A. G., Hutchinson, J. W. & Whitesides, G. M. Spontaneous formation of ordered structures in thin films of metals supported on an elastomeric polymer. *Nature* **393**, 146–149 (1998).
12. Bowden, N., Choi, I. S., Grzybowski, B. A. & Whitesides, G. M. Mesoscale self-assembly of hexagonal plates using lateral capillary forces: synthesis using the "capillary bond". *J. Am. Chem. Soc.* **121**, 5373–5391 (1999).
13. Shinbrot, T. Competition between randomizing impacts and inelastic collisions in granular pattern formation. *Nature* **389**, 574–576 (1997).
14. Burns, M. M., Fournier, J. M. & Golovchenko, J. A. Optical matter—crystallization and binding in intense optical fields. *Science* **249**, 749–754 (1990).
15. Murray, C. A. & Grier, D. G. Colloidal crystals—solid particles suspended in fluid form ordered arrays with unusual and useful physical properties. *Am. Sci.* **83**, 238–245 (1995).
16. Thompson, D'A. *On Growth and Form* (Dover, New York, 1992).
17. Shapiro, J. A. Thinking about bacterial populations as multicellular organisms. *Annu. Rev. Microbiol.* **52**, 81–104 (1998).
18. Berg, H. & Budrene, E. O. Dynamics of formation of symmetrical patterns by chemotactic bacteria. *Nature* **376**, 49–53 (1995).
19. GomezLopez, M., Preece, J. A. & Stoddart, J. F. The art and science of self-assembling molecular machines. *Nanotechnology* **7**, 183–192 (1996).
20. Koschmieder, A. *Benard Cells and Taylor Vortices* (Cambridge Univ. Press, New York, 1993).
21. Jakubith, S., Rotermund, H. H., Engel, W., von Oertzen, A. & Ertl, G. Spatiotemporal concentration patterns in a surface reaction: propagating and standing waves, rotating spirals, and turbulence. *Phys. Rev. Lett.* **65**, 3013–3016 (1990).
22. Engelborghs, Y. Microtubules—dissipative structures formed by self-assembly. *Biosens. Bioelectron.* **9**, 685–689 (1994).
23. Lindgren, K., Moore, C. & Nordahl, M. Complexity of two-dimensional patterns. *J. Stat. Phys.* **91**, 909–951 (1998).
24. Singh, R., Maru, V. M. & Moharir, P. S. Complex chaotic systems and emergent phenomena. *J. Nonlinear Sci.* **8**, 235–259 (1998).
25. Havelock, T. H. The stability of motion of rectilinear vortices in ring formation. *Phil. Mag.* **11**, 617–633 (1931).
26. Morton, W. B. Vortex polygons. *Proc. R. Irish Acad. A* **42**, 21–29 (1935).
27. Aref, H. & Vainchtein, D. L. Point vortices exhibit asymmetric equilibria. *Nature* **392**, 769–770 (1998).
28. Thomson, J. J. *A Treatise on the Motion of Vortex Rings* (Macmillan, London, 1883).
29. Dritschel, D. G. The stability and energetics of corotating uniform vortices. *J. Fluid Mech.* **157**, 95–134 (1985).
30. Schonberg, J. A. & Hinch, E. J. Inertial migration of a sphere in Poiseuille flow. *J. Fluid Mech.* **203**, 517–524 (1989).

Structural basis for the fracture toughness of the shell of the conch *Strombus gigas*

S. Kamat*, X. Su*, R. Ballarini† & A. H. Heuer*

* Department of Materials Science and Engineering, † Department of Civil Engineering, Case Western Reserve University, Cleveland, Ohio 44106-7204, USA

Natural composite materials are renowned for their mechanical strength and toughness: despite being highly mineralized, with the organic component constituting not more than a few per cent of the composite material, the fracture toughness exceeds that of single crystals of the pure mineral by two to three orders of magnitude[1]. The judicious placement of the organic matrix, relative to the mineral phase, and the hierarchical structural architecture extending over several distinct length scales both play crucial roles in the mechanical response of natural composites to external loads[2-4]. Here we use transmission electron microscopy studies and beam bending experiments to show that the resistance of the shell of the conch *Strombus gigas* to catastrophic fracture can be understood quantitatively by invoking two energy-dissipating mechanisms: multiple microcracking in the outer layers at low mechanical loads, and crack bridging in the shell's tougher middle layers at higher loads. Both mechanisms are intimately associated with the so-called crossed lamellar microarchitecture of the shell, which provides for 'channel' cracking in the outer layers and uncracked structural features that bridge crack surfaces, thereby significantly increasing the work of fracture, and hence the toughness, of the material. Despite a high mineral content of about 99% (by volume) of aragonite, the shell of *Strombus gigas* can thus be considered a 'ceramic plywood', and can guide the biomimetic design of tough, lightweight structures.

The crossed lamellar shell of *Strombus gigas*, the giant pink Queen conch native to Caribbean habitats, contains structure at five

distinct length scales. Other mollusc shell microarchitectures are nacreous, foliated, prismatic, homogeneous, and complex crossed lamellar[5,6], but the crossed lamellar structure is the most common one, and is associated with the highest nominal fracture toughness, K_{Ic} (refs 7–10). This fracture-mechanics parameter measures the resistance of a solid to crack propagation, and is directly related to the state of stress near the tip of a crack at the onset of crack extension. For perfectly brittle materials, the surface energy created during fracture, 2γ, determines the energetics of the fracture process. The fracture toughness and the effective Young's modulus, E, are then related to γ through the Irwin relation $K_{Ic} = \sqrt{2\gamma E}$. Tougher materials exhibit additional energy-dissipating fracture mechanisms; for shells with the crossed lamellar structure, the additional energy required for crack propagation, J, arises because the crack surfaces are bridged by microstructural features resulting from the unique microarchitecture.

The hierarchy of the structural features that comprise the shell of *Strombus gigas*, and their characteristic dimensions, are shown in Fig. 1a, a highly schematic drawing summarizing our current knowledge of the structure. The basic building blocks are third-order, aragonite (a polymorph of calcium carbonate, $CaCO_3$) lamellae, which are about 100 nm by 250 nm in cross-section, many micrometres long, internally twinned, and completely surrounded by organic matrix. The coarsest features are macro-scopic layers, which are best seen using scanning electron micro-scopy (SEM) of fractured surfaces of bend test specimens, Fig. 1b. Such specimens were taken from the last whorl of the shell, and contained three macroscopic layers. (The shell lip, which is present only in mature individuals, can contain more than three individual layers.) The higher-magnification images of the fracture surface, Fig. 1c and d, clearly show the first-order, second-order and third-order lamellae and their relative orientation, and fully justify the 'crossed lamellar' description of the microarchitecture.

Imaging of the organic matrix present in the lamellar interfaces in this heavily mineralized (~99% aragonitic $CaCO_3$) shell is necessary to understand its mechanics. Figure 2a shows a partially demineralized polished section, in which first-order (BCCB, BCB) and second-order (CC) lamellar interfaces can clearly be seen. Figure 2b, c and d show transmission electron microscopy (TEM) images of first-order, second-order, and third-order lamellar inter-faces, respectively. The judicious placement of the proteinaceous matrix surrounding and separating the several lamellar orders of the stiffer mineral phase profoundly affects the mechanical response of the shell.

During bending deformation, multiple channel cracks along first-order interfaces develop in the inner layer at low loads, but are arrested by the tough middle layer; catastrophic failure is mitigated until much higher loads. The mutual shielding produced by the interaction of these closely spaced cracks, which propagate along first-order lamellar interfaces, contributes to a higher stress for catastrophic failure (and in turn a higher work of fracture, which is given by the area under the stress–strain curve divided by the fracture surface area) compared to singly cracked specimens[10]. This aspect of the fracture response can be modelled[11] using a two-layer, elastically homogeneous structure with the fracture toughness of the middle layer, K_{Ic}^{m}, being λ times higher than that of the inner layer, K_{Ic}^{i}. For multiple cracks to develop under uniform tension, λ must be greater than 2. For λ as small as 3, a 20-fold increase in the work of fracture is achieved, together with an initiation stress that is three times higher than the stress required to fracture a specimen with a uniform toughness equal to that of the middle layer.

As the load is increased, a saturation channel crack density is eventually reached, and one or more of the channel cracks start to grow through the middle layer, along the interfaces between second-order lamellae. These cracks do not propagate catastrophically through the middle layer; instead they are retarded by the bridging action of the first-order lamellae. (Sometimes, they grow for a short distance along the interface between the inner and middle layers before traversing the middle layer.) As discussed next, this
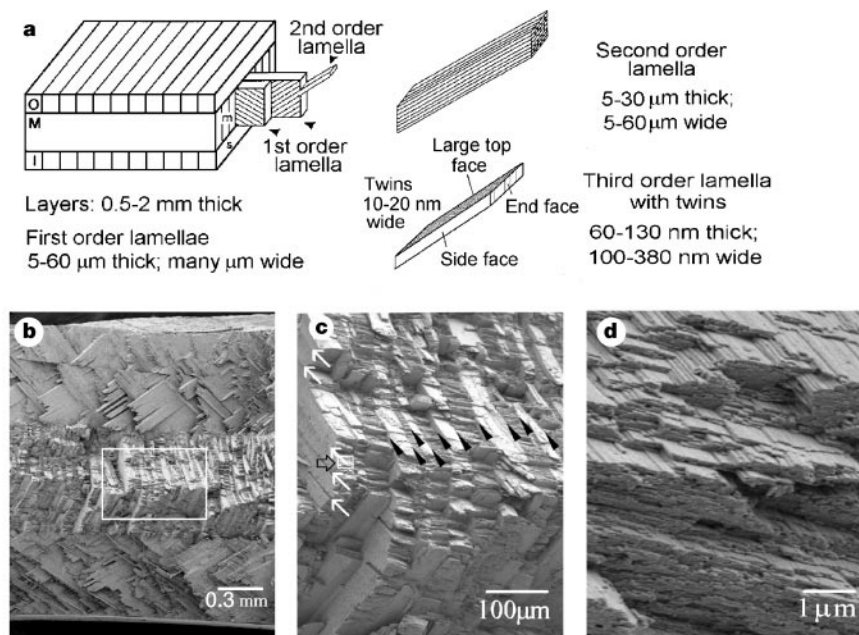

Figure 1 Microarchitecture of the shell of *Strombus gigas*. **a**, A schematic drawing of the crossed lamellar microarchitecture, including characteristic dimensions of the three lamellar orders. (O, M and I refer to outer, middle and inner (adjacent to the animal) layers, respectively.) **b, c** and **d**, SEM images of the fracture surface of a bend specimen taken at increasing magnification (the boxed areas in **b** and **c** (see open arrow in **c**) are shown in **c** and **d**, respectively). The first- and second-order interfaces can be clearly seen and are indicated by black arrowheads and white arrows, respectively, in **c**. Third-order lamellae are readily observed in **d**. The organic matrix cannot be discerned in such images; visualizing the matrix requires transmission electron microscopy (see Fig. 2b–d).

phenomenon is responsible for ultimate load and work of fracture values that are significantly higher than those that would result from the propagation of unbridged cracks (as assumed by the simple two-layer linear model).

Damage associated with catastrophic fracture is shown in Fig. 3. A surface inclined to a strength-defining crack within a fractured specimen is shown in Fig. 3a; the geometry is sketched in Fig. 3b. As the crack front cleaves the interfaces between second-order lamellae, every other first-order lamella remains intact, and contributes to the reduction of the crack opening displacement (COD). The net bridging tractions on the strength-defining crack are influenced by the stiffness of the first-order lamellae, as well as by the frictional stress along the interfacial cracks that develop along the parallel interfaces between first-order lamellae.

Figure 3c and d shows microcracks within the middle layer of a fractured, dye-impregnated sample; the micrograph was obtained by polishing away the outer layer. The load–displacement curve for this specimen, shown in Fig. 3e, clearly illustrates the onset of channel cracking, interlayer delamination, and the high work of fracture of the shell.

Notched fracture-mechanics bend specimens were also prepared, as shown in Fig. 4a. For initial machined notches confined to the inner layer, the crack front propagated self-similarly along the first-order lamellar interfaces. For those samples containing notches machined into the middle layer, cracks propagated directly along the second order interfaces at ~45° to the applied flexural tensile stress. (Some specimens developed short delamination cracks at the interface between the inner and middle layers.) The inset in Fig. 4a presents the nominal fracture toughness and its standard deviation derived from these tests. For initial notches in the inner layer, these values represent the toughness of the protein interface; for those in the middle layer, they represent an effective initiation toughness of the middle layer.

We note two points about these data: the negligible difference in interface toughness between wet and dry specimens, and the approximately four times difference in toughness between the inner and middle layers. This last point is consistent with the requirement derived from the multiple cracking model[11]; $\lambda > 2$ results in multiple channel cracks. However, the multiple channel-cracking model cannot predict the ultimate load and work of fracture (and their dependence on shell dimensions), because crack propagation in the middle layer is not accurately characterized by a constant K_{lc}^m. Instead, it is associated with a form of crack bridging that is analogous to fibre bridging in fibrous composites, as we now show.

Load–displacement curves for specimens in which the cracks extended into the middle layers can be used to calibrate a micro-mechanics crack-bridging model, which can then be used to predict the effects of shell dimensions on ultimate load and work of fracture. (Previous work[8–10] contained critical nominal stresses and work of fracture for varying shell dimensions, with no rationally derived relationships that could generate structural predictions.) Such
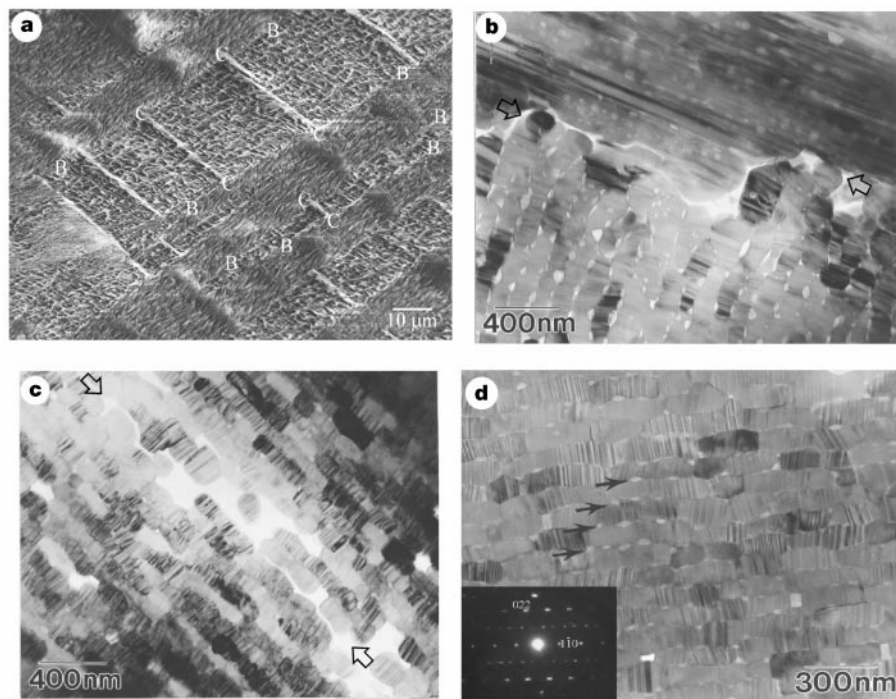

Figure 2 Images of shell specimens that show lamellar interfaces. **a**, SEM image of a polished, partially demineralized shell section showing interfaces separating second-order lamellae (CC) and interfaces separating first-order lamellae (BCCB and BCB). The long axes of the third-order lamellae are at an angle of about 45° to this polished section. These images confirm previous claims[8] that the organic matrix surrounds every crystallite and is present at every interface. However, the boundaries of the second-order lamellae are thicker than the boundaries separating first-order lamellae. Within any second-order lamella, protein matrix associated with third-order lamellae can also be seen. **b**, **c,** TEM micrographs of ion-thinned specimens showing a first-order interface in **b**, and a second-order interface in **c** (the arrowed feature in each image). The interface thickness varies from 10 to 220 nm for the first-order interfaces and 20 to 320 nm for the second-order interfaces. It is clear that adjacent first-order lamellae are misoriented by ~90°, and that the side faces of the third-order lamellae (see Fig. 1a) are parallel to the first-order interfaces. On the other hand, adjacent second-order lamellae are not misoriented; rather, the interfaces between adjacent lamellae are thicker regions of matrix, even thicker than the first-order planar interfaces. At the scale visible in the TEM, first-order lamellar interfaces are neither flat nor planar. **d**, TEM end-face image, also of an ion-thinned specimen. The protein sheaths present between third-order lamellae are made up of thin membrane-like organic sheets connected to thicker globular proteins. (That these were proteinaceous and not empty space was confirmed by chemical microanalysis using electron energy-loss spectroscopy, EELS). The globular features are arranged along the top and bottom of each third-order lamella but not along the sides of these lamellae. The inset diffraction pattern reveals that the vertical features present in every third-order lamella are 'polysynthetic' growth twins.
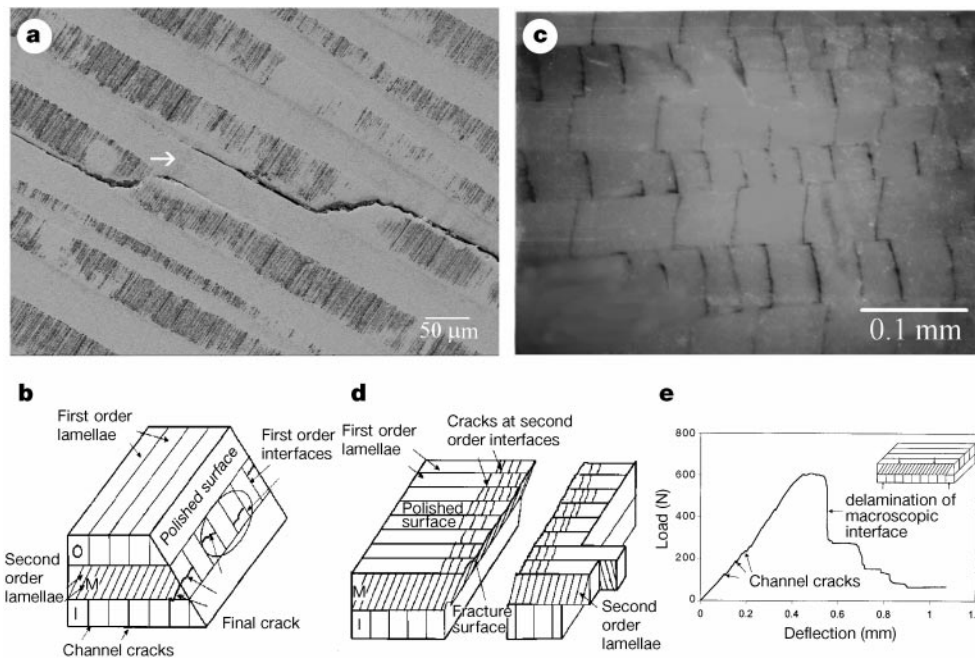
Figure 3 Damage development in the shell of *Strombus gigas* due to the difficulties of crack propagation within the middle layer. **a**, SEM image of a fractured specimen that underwent graceful, that is, non-catastrophic, failure and was intact after removal from the testing machine; a plane inclined to that of the strength-defining crack was then polished. **b**, Schematic drawing that shows that the crack penetrated every other first-order lamella, propagating long distances between the favourably and unfavourably oriented lamellae. In the arrowed region in **a**, the crack was unable to penetrate the first-order lamella and caused delamination at the first-order interface. **c**, Optical micrograph (reflected light) showing stained microcracks within the middle layer of a failed sample near the final crack after dye penetration and serial sectioning, while **d** shows the fracture geometry. This microcracking within the middle layer accompanying final failure was restricted to a region ~1 mm from the plane of the final crack. **e**, Load–deflection curve for the specimen of **c**. The occurrence of channel cracks and layer delamination is evident in the load–deflection curve.
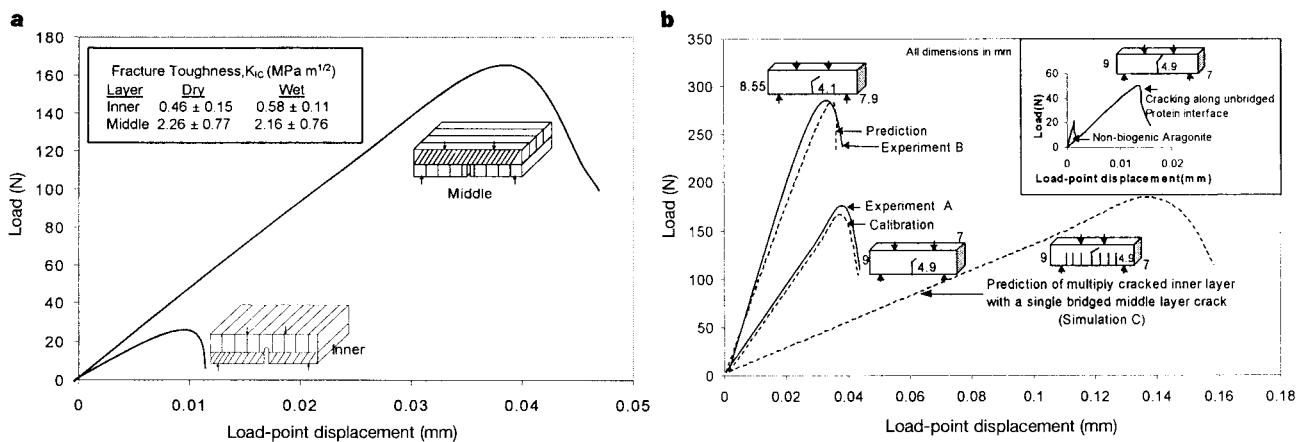

Figure 4 Load–displacement curves of notched bend test specimens. **a**, Curves measured on test specimens where the initial notch tip was machined either into the inner layer or into the middle layer. The inset in **a** shows the average fracture toughness K_{Ic} and its standard deviation, calculated from the peak loads for dry samples and for those tested wet after storing in artificial sea water for 30 days. **b**, Experimental and theoretical load–deflection curves for specimens containing middle layer notches. The 'calibration' sample A allows determination of the parameters of the crack bridging model, and suggests that β = 630 N mm$^{-5/2}$ and COD$_{cr}$ = 5 μm. These parameters allow good prediction of the load–deflection response for a specimen (B) with different geometry. Comparing the theoretical unnotched beam response (simulation C, involving multiple cracking followed by a single channel crack propagating through the bridged middle layer) with the theoretically predicted response of beams comprised solely of non-biogenic aragonite (K_{Ic} = 0.25 MPa m$^{1/2}$) or a beam in which cracks propagate unbridged along a mineral–protein interface (K_{Ic} = 0.6 MPa m$^{1/2}$) shown in the inset clearly illustrates the impressive fracture toughness of the shell of *Strombus gigas*. In the crack-bridging model, equilibrium configurations are calculated under the assumption that the strength-defining crack is bridged according to the previously defined cohesive tractions, and extends at a stress intensity factor equal to the toughness of the mineral–protein interface.

letters to nature

nonlinear fracture mechanics theories[12] approximate, through tractions that resist crack opening, the net effects of various bridging mechanisms, such as bridging and frictional sliding between first-order lamellae and microcracking. Our micromechanical model predicts that the magnitudes of the bridging stresses, p, are proportional to the square root of the COD ($p = \beta \sqrt{\text{COD}}$), and are operative up to a critical opening COD_{cr}; here, β incorporates the effects of all possible energy-dissipating mechanisms. The additional energy associated with a fully developed bridging zone (whose tail has reached COD_{cr}) is given as:

$$J = \int_0^{(\text{COD}_{cr})} p(\text{COD}) d(\text{COD}) = \frac{2}{3} \beta (\text{COD}_{cr})^{3/2}$$

We note that in this type of theory, which has been successful with other brittle matrix composites[12], the bridging law is the true material property.

Figure 4b shows load–displacement curves for a notched specimen (experiment A) and the 'calibration' simulation; a good fit to experiment is obtained using $\beta = 630 \, \text{N m}^{-5/2}$ and $\text{COD}_{cr} = 5 \, \mu\text{m}$ ($J = 0.15 \, \text{N mm}^{-1}$). A comparison between the predictions of the now-calibrated bridging model and the experimental response of a notched beam of different dimensions (experiment B) is also shown in Fig. 4b. The model accurately predicts the behaviour of cracks propagating through the middle layer, and in turn, the effects of shell dimensions. The model can also predict the response of a multiply cracked unnotched shell sample, where final fracture results from the (stochastic) propagation through the middle layer of a single channel crack (simulation C). The load–deflection curve for this case suggests that the combination of multiple cracking and 'fibre' bridging increases the work of fracture by an additional order of magnitude.

A comparison of this last simulation with the mechanical response predicted for a crack growing self-similarly in a pure aragonite shell, or for a crack growing at 45° along an unbridged protein interface (see the inset of Fig. 4b) emphasizes the truly impressive fracture toughness of the shell of *Strombus gigas*. We consider that the microarchitecture of the *Strombus gigas* shell—that is, 'ceramic plywood'—could guide the design of lightweight structural composites. □

1. Wegst, U. G. K. & Ashby, M. F. Material selection charts for natural materials. Report No. CUED/C_EDC/TR55 (Cambridge Univ., 1997).
2. Taylor, J. D. & Layman, M. The mechanical properties of bivalve (mollusca) shell structures. *Palaeontology* **15**, 73–86 (1972).
3. Currey, J. D. & Taylor, J. D. The mechanical behaviour of some molluscan hard tissue. *J. Zool. Lond.* **173**, 395–406 (1974).
4. Currey, J. D. in *Mechanical Properties of Biological Materials* (eds Currey, J. D. & Vincent, J. F. V.) 75–97 (Cambridge Univ. Press, 1980).
5. Bøggild, O. B. The shell structure of the mollusks. *K. Danske Vidensk. Selsk. Skr.* **2**, 232–325 (1930).
6. Carter, J. G. in *Skeletal Growth of Aquatic Organisms* (eds Rhoads, D. C. & Lutz, R. A.) 69–113 (Plenum, New York, 1980).
7. Curry, J. D. & Kohn, A. J. Fracture in the crossed-lamellar structure of *Conus* shells. *J. Mater. Sci.* **11**, 1615–1623 (1976).
8. Jackson, A. P., Vincent, J. F. V. & Turner, R. M. The mechanical design of nacre. *Proc. R. Soc. Lond. B* **234**, 415–440 (1988).
9. Jackson, A. P., Vincent, J. F. V. & Turner, R. M. Comparison of nacre with other ceramic composites. *J. Mater. Sci.* **25**, 3173–3178 (1990).
10. Kuhn-Spearing, L. T., Kessler, H., Spearing, S. M., Ballarini, R. & Heuer, A. H. Fracture mechanisms of the *Strombus gigas* conch shell: Implication for the design of brittle laminates. *J. Mater. Sci.* **31**, 6583–6594 (1996).
11. Kessler, H., Ballarini, R., Mullen, R. L., Kuhn, L. T. & Heuer, A. H. A biomimetic example of brittle toughening: (I) steady state multiple cracking. *Comput. Mater. Sci.* **5**, 157–166 (1996).
12. Cox, B. & Marshall, D. B. Concepts for bridged cracks in fracture and fatigue. Overview No. 111. *Acta Metall. Mater.* **42**, 341–363 (1994).

Palaeotemperature reconstruction from noble gases in ground water taking into account equilibration with entrapped air

W. Aeschbach-Hertig*†, F. Peeters*, U. Beyerle* & R. Kipfer*‡

Department of Water Resources and Drinking Water, Swiss Federal Institute of Environmental Science and Technology (EAWAG), CH-8600 Dübendorf, Switzerland
†*Environmental Physics, ‡Isotope Geology, Swiss Federal Institute of Technology (ETH), CH-8902 Zurich, Switzerland*

Noble-gas concentrations in ground water have been used as a proxy for past air temperatures[1-7], but the accuracy of this approach has been limited by the existence of a temperature-independent component of the noble gases in ground water, termed 'excess air', whose origin and composition is poorly understood[7-9]. In particular, the evidence from noble gases in a Brazilian aquifer for a cooling of more than 5 °C in tropical America during the Last Glacial Maximum[4] has been called into question[9]. Here we propose a model for dissolved gases in ground water, which describes the formation of excess air by equilibration of ground water with entrapped air in quasi-saturated soils[10-12]. Our model predicts previously unexplained noble-gas data sets, including the concentration of atmospheric helium, and yields consistent results for the non-atmospheric helium isotopes that are used for dating ground water. Using this model of excess air, we re-evaluate the use of noble gases from ground water for reconstructing past temperatures. Our results corroborate the inferred cooling in Brazil during the Last Glacial Maximum[4], and indicate that even larger cooling took place at mid-latitudes.

Noble gases in ground water consist of three components: (1) dissolved air at solubility equilibrium, (2) certain isotopes from radioactive decay[13], and (3) "excess air"[8]. The temperature dependence of the first component has been used to infer recharge temperatures of ground water in order to reconstruct palaeotemperatures[1-7]. The second component is of importance for He (^{3}He from ^{3}H, ^{4}He from U/Th), and has been used extensively for groundwater dating[14-19]. Little is known about the origin and composition of the third component, although excess air may contain information about the environmental conditions pertaining during infiltration[7,20-22]. An understanding of the excess-air phenomenon is needed for the reliable calculation of noble-gas temperatures (NGTs) and groundwater ages.

Usually it is assumed that excess air is formed by total dissolution

Table 1 Statistical analysis of fits of excess-air models to noble-gas data sets

Data set	N	TD model χ^2	TD model P	PR model χ^2	PR model P	CE model χ^2	CE model P
Brazil	20	626.4	$< 10^{-14}$	71.8	9×10^{-8}	35.8	0.016
Oman	9	153.0	$< 10^{-14}$	55.2	1×10^{-8}	20.4	0.016
Maryland	20	246.8	$< 10^{-14}$	44.5	0.001	18.2	0.574
Belgium	28	303.6	$< 10^{-14}$	55.7	0.001	12.8	0.994
Belgium He*	28	358.6	$< 10^{-14}$	191.5	1×10^{-14}	34.2	0.990

N is the number of samples of each data set. χ^2 is the sum of the weighted squared deviations between modelled and measured noble-gas concentrations, summed over all samples of a data set[9,23]. The expected value of χ^2 is equal to the number of degrees of freedom, which is the number of fitted concentrations (4N, with He 5N) minus the number of free model parameters (2N (T, A_d) for the TD model, 3N (T, A_d, R or T, A_e, F) otherwise). P is the probability that χ^2 exceeds the observed value. Models with $P < 0.01$ are rejected.
* Belgian data set with the calculated He$_{atm}$ (Methods, Fig. 1) as additional constraint.